C. RADIONUCLIDE TRANSPORT THROUGH FRACTURES

Yucca Mountain was chosen as a potential site for a high-level nuclear-waste repository because its geochemistry is believed to form both a physical as well as chemical barrier to radionuclide migration. However, the Yucca Mountain region has undergone significant deformation with the most recent tectonic activity occurring during the development of the Basin and Range geologic province and silicic volcanic activity. As a result of the tectonics and volcanism, many faults and fractures were produced within the tuffaceous units as well as the entire region. In addition, volcanic tuffs are often fractured as a result of cooling. The numerous fractures present at Yucca Mountain potentially represent a breach in the natural barrier, providing a fast pathway for contaminant migration.

Radionuclide transport calculations often assume that radionuclides can travel through fractures unimpeded; this assumption is too simplistic and leads to overconservative predictions of radionuclide releases to the accessible environment. The assumption ignores two main mechanisms by which retardation of radionuclides migrating through fractures can occur: diffusion of the radionuclides from the fractures into the rock matrix and sorption of radionuclides onto the minerals coating the fractures.

Minerals coating the fracture walls are generally different from the host-rock mineralogy due to a variety of factors ranging from precipitation of hydrothermal waters or meteoric waters to alteration of the pre-existing minerals. A review of the literature (Carlos 1985, 1987, 1989, 1990, 1994; Carlos et al. 1993) has provided a list of the minerals lining the fractures found at Yucca Mountain (Table 29 and see Appendix A for detailed descriptions).

The transport of radionuclides through fractures from Yucca Mountain was examined to assess the retardation that can be provided by radionuclide diffusion into the matrix and sorption onto the minerals coating the Yucca Mountain fractures.

Experimental Procedures

Groundwaters

The groundwaters used for the experiments presented in this section were waters from Well J-13 (filtered through a 0.05-μm filter) and two sodium-bicarbonate buffers that simulated the water chemistry of the groundwaters from Wells J-13 and UE-25 p#1. We prepared the synthetic J-13 water by dissolving 0.03 g of Na_2CO_3 and 1.92 g of $NaHCO_3$ in 10 l of deionized water; the synthetic UE-25 p#1 water by dissolving 0.39 g of Na_2CO_3 and 8.90 g of $NaHCO_3$ in 10 l of deionized water. The reasons for having to use synthetic waters for the fracture-column experiments was the unavailability of water from Well UE-25 p#1 and the prevention of microbial activity in the columns.

Fractured-tuff samples

We used tuff samples with natural fractures from drill holes at Yucca Mountain chosen from the Yucca Mountain Project Sample Management Facility (SMF) in Mercury, Nevada. The tuff matrix of all samples consisted of devitrified tuff, and the minerals lining the fractures were stellerite, magnetite, hollandite, and romanechite. The sampling criteria was confined to 1) cores with natural fractures, determined by the presence of secondary mineral coatings, and 2) fractures with removable fracture walls that could be repositioned to their original orientation. Based on this criteria, we concluded that of the fractured-tuff cores selected (USW G1-1941, UE-25 UZ-16 919, USW G4-2981, and USW G4-2954) all consisted of natural fractures except G1-1941, the only core sample that did not have secondary minerals coating its fracture. The fracture in sample G1-1941 is apparently induced.

Radionuclide solutions

The radionuclide solutions used in the experiments (tritium, pertechnetate, and neptunium) were prepared in the same manner as for the crushed-tuff

Table 29. Minerals Coating Fracture Walls in Yucca Mountain Tuffs

---

Zeolites

Heulandite ⟷ Clinoptilolite $Ca_4Al_8Si_{28}O_{72} \cdot 24H_2O$ ⟷ $(Na, K)_6Al_6Si_{30}O_{72} \cdot 24H_2O$

   (range of compositions with arbitrary division of Si/Al < 4.4 for heulandite and Si/Al > 4.4 for clinoptilolite)

Mordenite	$(Ca,Na_2,K_2)_4Al_8Si_{40}O_{96} \cdot 28H_2O$
Analcime	$NaAlSi_2O_6 \cdot H_2O$
Chabazite	$CaAl_2Si_4O_{12} \cdot 6H_2O$
Phillipsite	$(K_2,Na_2,Ca)Al_2Si_4O_{12} \cdot 4–5H_2O$
Erionite	$(Ca,Na_2,K_2)_4Al_8Si_{28}O_{72} \cdot 27H_2O$
Stellerite	$CaAl_2Si_7O_{18} \cdot 7H_2O$

Silica

Quartz	SiO_2 — low-temperature polymorph of silica
Tridymite	SiO_2 — high-temperature polymorph of silica
Cristobalite	SiO_2 — highest-temperature polymorph of silica
Opal	$SiO_2 \cdot nH_2O$
Feldspars	
Plagioclase (albite)	Solid solutions of albite ($NaAlSi_3O_8$) and anorthite ($CaAl_2Si_2O_8$)
K-feldspar (sanidine)	Solid solutions of orthoclase ($KAlSi_3O_8$) and albite ($NaAlSi_3O_8$)

Clays

Smectite family:	
Dioctahedral (montmorillonite)	$(Na,K,Mg_{0.5},Ca_{0.5},\text{possibly others})_{0.33}Al_{1.67}Mg_{0.33}Si_4O_{10}(OH)_2 \cdot nH_2O$
Trioctahedral (saponite)	$(Ca_{0.5},Na)_{0.33}(Mg,Fe)_3(Si_{3.67}Al_{0.33})O_{10}(OH)_2 \cdot 4H_2O$
Sepiolite	$Mg_4(Si_2O_5)_3(OH)_2 \cdot 6H_2O$
Palygorskite	$(Mg,Al)_2Si_4O_{10}(OH) \cdot 4H_2O$
Illite	$(H_3O,K)_y(Al_4Fe_4Mg_4Mg_6)(Si_{8-y}Al_y)O_{20}(OH)_4$

Manganese oxides/hydroxides

Pyrolusite	MnO_2	(1 × 1 tunnel structure)
Cryptomelane family:	$A_{0-2}(Mn^{4+},Mn^{3+})_8(O,OH)_{16}$	(2 × 2 tunnel structure)
Cryptomelane	$A = K$	
Hollandite	$A = Ba$	
Coronadite	$A = Pb$	
Romanechite	$(Ba,H_2O)_2Mn_5O_{10}$	(2 × 3 tunnel structure)
Todorokite	$(Na,Ca,Ba,Sr)_{0.3-0.7}(Mn,Mg,Al)_6O_{12} \cdot 3.2–4.5H_2O$	(3 × 3 tunnel structure)
Aurorite	$(Mn^{2+},Ag,Ca)Mn_3O_7 \cdot 3H_2O$	
Lithiophorite	$m\{Al_{0.5}Li_{0.5}MnO_2(OH)_2\} \cdot n\{Al_{0.667}(Mn^{4+},Co,Ni,Mn^{2+})O_2(OH)_2\} \cdot pH_2O$	
Rancieite	$(Ca,Mn^{2+})(Mn^{4+})_4O_9 \cdot 3H_2O$	

Iron oxides/hydroxides

Hematite	Fe_2O_3
Magnetite	$(Fe,Mg)Fe_2O_4$

Carbonates

Calcite	$CaCO_3$

Halides

Fluorite	CaF_2

column experiments.

Fractured-column procedure

The experimental setup that we used for the fractured-tuff column is shown in Fig. 119 (the flow chart for the experiments is the same as for the crushed-tuff column experiments (Fig. 97), except the crushed-rock column is replaced with a fractured-tuff column). The fractured cores we chose for column experiments were cut with a rock saw perpendicular to the fracture to produce smooth ends. The fracture was secured with a hoseclamp, and we measured and logged the dimensions of the fracture and the core for all samples.

We made round endcaps for the fracture columns from 1/2- to 1-inch flat Plexiglas™. The diameter of the endcaps was slightly larger than the core by approximately 1/8 inch to produce an overlip. We cored the endcaps within the overlip to a depth of 1/16 to 1/8 inch with the exact diameter of the rock core and then fitted them onto the core. We drew a trace of the fracture on the caps with a marking pen and, using a mill, cut 1/16-inch-deep troughs over the designated area. The purpose of the troughs was to induce equal dispersion of the tracer through the fracture at the time of the injection rather than creating a point injection. We also milled two areas (resembling opposing D's) 1/8 inch outside both sides of the trough, 1/8 inch from the cored overlip, and with the same depth as the troughs.

Next, we drilled two 1/16-inch holes through the troughs of each endcap to act as the inlet and outlet flow ports for the columns. The top of each hole was redrilled to a depth of 1/4 inch and tapped to a 1/4-by-28 thread. We secured the endcaps to the fracture by placing a thin coating of Silastic™ within the over-

lip and the milled D-sections.

Silastic was also spread over all exposures of the rock core, including the fracture, and allowed to cure completely. We selected a tube of transparent Lucite™ with a diameter greater than that of the endcaps, and cut it to a length measured betweeen the middle of both endcaps. A piece of Plexiglas, similar in thickness to the endcaps, was then cut in donut form so that it would fit between the Lucite
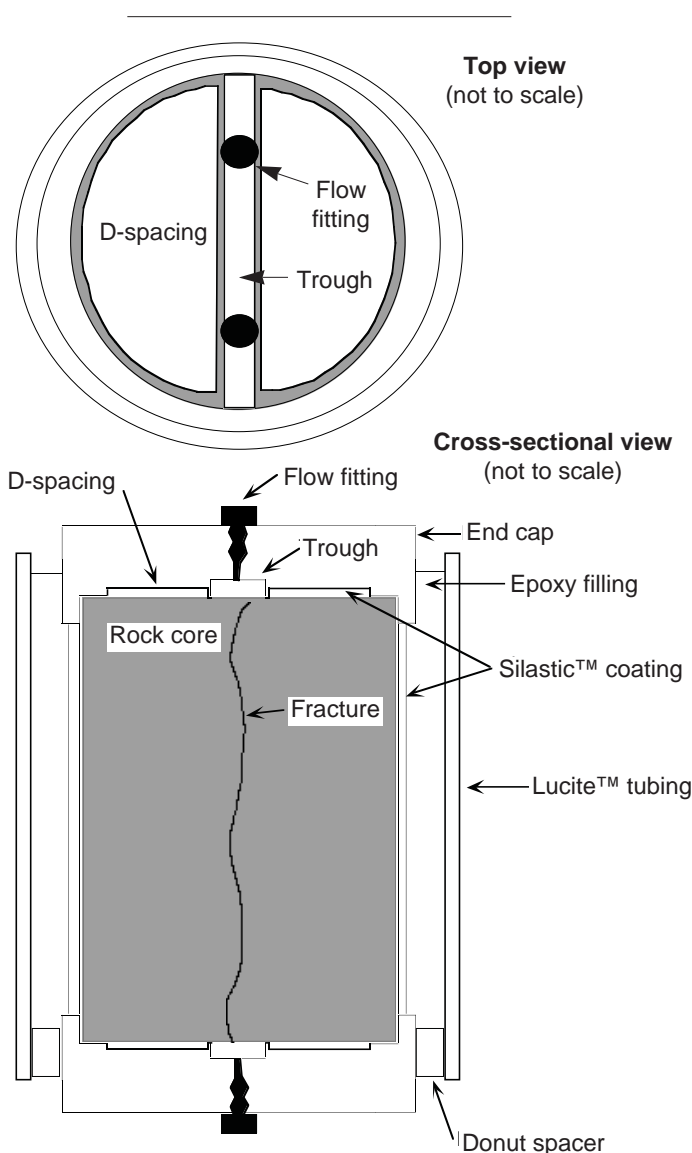

Figure 119. Fractured-column Setup. Top view (top) and cross-sectional view (bottom) of the column used in the fracture transport experiments.

tube and the endcaps. The resulting donut spacer was then pressed and sealed with Silastic to one end of the fracture column. We poured epoxy into the top of the column through the gap from the Lucite tubing and the endcap until it almost over-flowed the tube.

After all the epoxy cured, we flushed the column with carbon-dioxide gas for thirty minutes to facili-tate removal of insoluble nitrogen gas. Then the column was submerged in a beaker containing either synthetic UE-25 p#1 or synthetic J-13 water. We subjected the beakers to a vacuum for a mini-mum of two weeks until all evacuating gas bubbles had ceased. After saturation, we connected the fracture columns, via one of the two outflow ports, to a syringe pump. The purpose of the second out-flow port was to connect to a pressure transducer.

We then set the columns onto ring stands so that tracer could be injected through the bottom. This setup was done so that if gas bubbles developed they would rest at the top of the column's trough and not against the fracture. A constant flow rate was established, and then we introduced a radionu-clide tracer into the system through an injection valve. We collected the column elutions as a func-tion of time and analyzed them, using our standard radiometric techniques, for the percentage of radionuclide tracer recovered. The aperture of the fractures has not yet been determined, but Table 30 gives the other characteristics of the four columns.

Batch-sorption experiments

For comparison with the fractured-column experi-ments, we conducted batch-sorption tests of neptu-nium onto the fracture minerals stellerite, hollan-

Table 30. Characteristics of Fractured Devitrified-tuff Columns

	Column #1	Column #2	Column #3	Column #4
Tuff type	G1-1941	UE-25 UZ-16 919	G4-2981	G4-2954
SMF number	N/A	0029365	0029366	0029368
Major minerals in tuff matrix	Alkali Feldspar and Quartz	Alkali Feldspar and Quartz	AlkaliFeldspar and Opal CT	Alkali Feldspar and Opal CT
Minerals coating the fracture	None (apparent induced fracture)	Stellerite Magnetite	Hollandite Romanechite	Hollandite Romanechite
Water type	Synthetic J-13	Synthetic UE-25 p#1	Synthetic J-13	Synthetic J-13
pH	8.6	8.8	8.6	8.6
Concentration of ^{237}Np (M)	1.4×10^{-5}	4.8×10^{-6}	1.4×10^{-5}	1.4×10^{-5}
Length (cm)	12.6	6.1	6.0	To be determined
Diameter (cm)	6.1	5.2	5.2	To be determined
Fracture aperture	To be determined	To be determined	To be determined	To be determined
Porosity	To be determined	To be determined	To be determined	To be determined
Volumetric flow rate (ml/hr)	0.5	0.5	0.5	0.5

dite, romanechite, and magnetite. We did these tests under atmospheric conditions using J-13 well water with a Np(V) concentration of 6.7×10^{-7} M. The batch-sorption tests consisted of crushing and wet-sieving the minerals to a size of 75 to 500 μm, pretreating the minerals with J-13 water, placing the neptunium solution in contact with the minerals for a period of 3 days (using a solid to solution ration of 1 g to 20 ml), separating the phases by centrifugation, and determining the amount of neptunium in each phase by difference using liquid scintillation counting. We used control samples to determine the sorption of neptunium onto the walls of the sorption containers. The control samples consisted of following the described batch-sorption procedure with a sample containing the neptunium solution only with no solid added. The results of the control experiments indicate no loss of neptunium due to precipitation or sorption onto the walls of the container during the batch-sorption experiment. The pH of the water in these experiments was approximately 8.5.

Results and Discussion

As discussed earlier, neptunium does not sorb onto devitrified tuff (for example, see Table 15, p. 87, or Triay et al. 1996a), which constitutes the matrix of all the fractures studied. Retardation during fracture flow occurs by diffusion of the radionuclides into the tuff matrix or by sorption of the radionuclides onto the minerals coating the fractures. Table 31 lists the results of batch-sorption experiments describing the sorption of neptunium onto natural minerals.

Although the extrapolation from these experiments to Yucca Mountain tuffs containing the same minerals is not immediate, the data of Table 31 show some important trends. Neptunium has a high affinity for hollandite and romanechite, whereas sorption onto the zeolite stellerite is not significant. If ion exchange is the main mechanism for neptunium sorption onto stellerite, changing the water from J-13 to UE-25 p# 1 will only result in less sorption (due to the formation of a larger

amount of the neptunyl carbonato complex and competitive effects as a result of the higher ionic strength in the UE-25 p# 1 water). The sorption of neptunium onto magnetite does not appear to be significant either. As shown in Table 31, the magnetite sample we studied contains hematite and goethite, which could account for the entire observed sorption (Triay et al. 1996a).

Because no secondary minerals coating the fractures were observed for the G1-1941 fractured sample (column #1 of Table 30 and Fig. 120), it can be concluded that the retardation of neptunium observed for that column is due to diffusion into the matrix.

The total neptunium recovery of 70% in the UE-25 UZ-16 919 fractured sample (column #2 of Table 30 and Fig. 121) could be due to minimal sorption onto the stellerite and magnetite coating that fracture or due to diffusion into the matrix. It is important to note that in changing the water for this column from synthetic J-13 to synthetic UE-25 p#1, the speciation of neptunium changes from a mixture of neptunyl and carbonato complex to almost 100% carbonato complex (which can be excluded from tuff pores due to size and charge).

Neptunium seems to be significantly retarded even

Table 31. Batch-sorption Results for ^{237}Np in J-13 Well Water

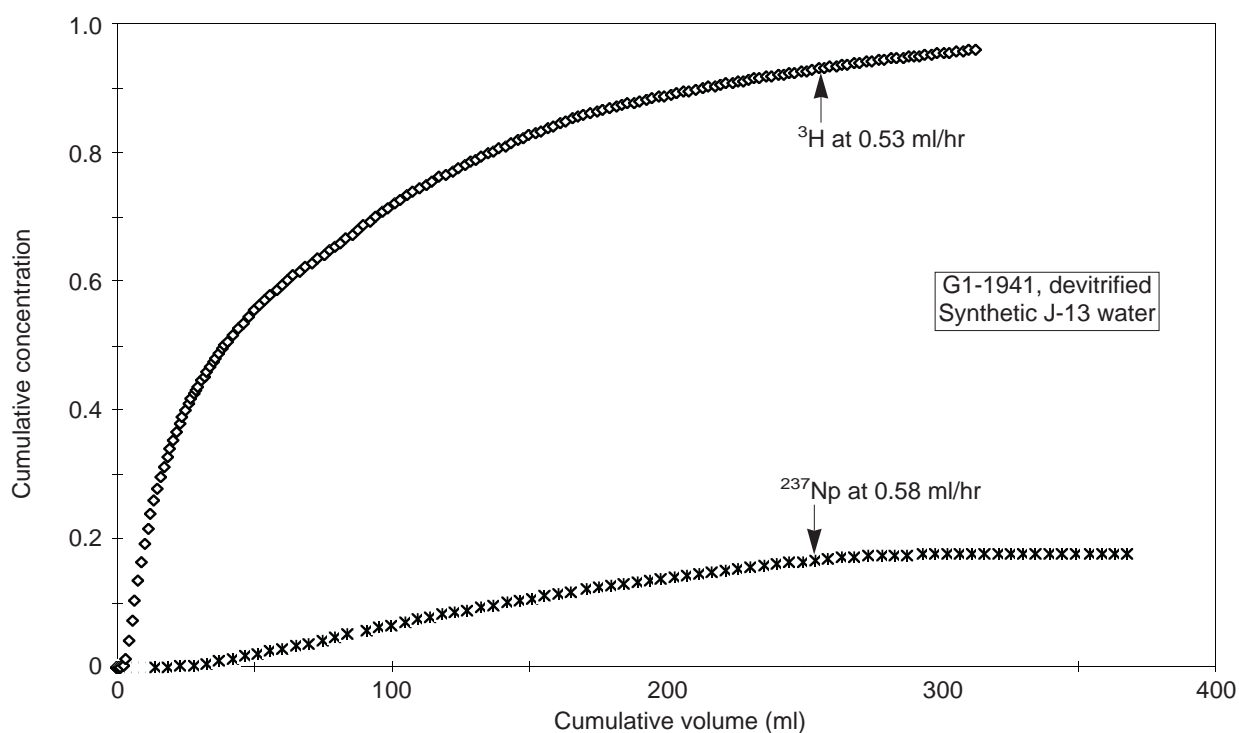| Major mineral in solid phase	K_d (ml/g)	Solid-phase composition*
Stellerite	~ 0	N/A
Hollandite	700	100% Hollandite
Romanechite	600	N/A
Magnetite	7	85% Magnetite 12% Hematite 3% Goethite

*determined by x-ray-diffraction analysis

Figure 120. Neptunium in Fractured Tuff. This plot shows the elution curves for tritium and neptunium-237 in synthetic J-13 water through a fractured-column of devitrified tuff sample G1-1941.
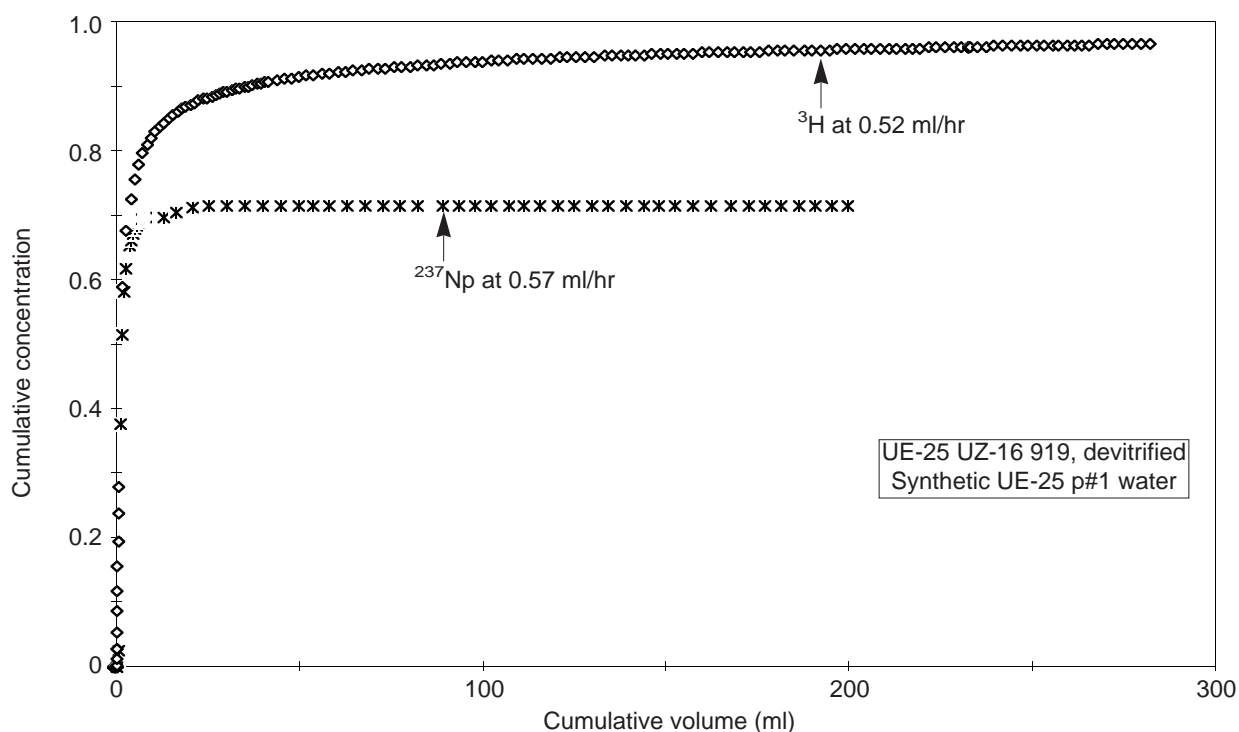

Figure 121. Neptunium in Fractured Tuff. This plot shows the elution curves for tritium and neptunium-237 in synthetic UE-25 p#1 water through a fractured-column of devitrified tuff UE-25 UZ-16 919.

165

during fracture-flow in the G4-2981 fractured sample (Fig. 122) that is coated with hollandite and romanechite. The recovery of neptunium in this fracture is less than 10%, and its first appearance is delayed with respect to tritium and technetium.

Inspection of Figs. 122 and 123 (columns #3 and #4 of Table 30) indicates that diffusion from the fracture into the matrix has taken place because recovery of tritium was only 80% compared to 90% for technetium. This trend agrees with diffusion data that was previously obtained for ^{3}H and ^{95m}Tc in devitrified tuff and water from Well J-13. These data were fitted to the diffusion equation using the transport code TRACRN (Triay et al. 1993a), which yielded diffusion coefficients for saturated devitrified tuffs that were of the order of 10^{-6} cm^2/s for tritiated water and 10^{-7} cm^2/s for technetium. Thus, anion exclusion, in which the large pertechnetate anion is excluded from tuff pores due to its size and charge, has been previously observed.

Continuing with the explanation by de Marsily (1986, Chapter 10) of the fate of reactive and non-reactive solutes in porous and fractured media that we started in the earlier section on crushed-rock columns, we can expand the equation for a sorbing, nonreactive solute (Eqn. 42) to account for a solute that also undergoes radioactive decay:

$$\nabla \cdot (\mathbf{D}C - C\mathbf{U}) =$$
$$\epsilon\left(\frac{\partial C}{\partial t} + \lambda C\right) + \rho_b\left(\frac{\partial F}{\partial t} + \lambda F\right) , \quad (49)$$

where λ is related to the half-life, $t_{1/2}$, of the decaying radionuclide by the relationship $\lambda = 0.693/t_{1/2}$.

As was pointed out earlier, the mechanism of sorption determines the relationship between F and C. If we substitute the linear, reversible, and instantaneous relationship for sorption, that is $F = K_d C$, then Eqn. 49 becomes

$$\nabla \cdot (\mathbf{D}C - C\mathbf{U}) =$$
$$\epsilon\left(1 + \frac{\rho_b}{\epsilon}K_d\right)\left(\frac{\partial C}{\partial t} + \lambda C\right) . \quad (50)$$

The expression inside the first set of parentheses in Eqn. 50 is the retardation factor, R_f, which, of course, is only valid if sorption is linear, reversible, and instantaneous.

For radionuclide elution through fractures, two transport equations (like Eqn. 49) are considered, one for the porous medium and one for the fractured medium, each with its own Darcy's velocity and porosity (de Marsily 1986). The two transport equations for the porous and the fractured media can be coupled by a convection and a dispersion-exchange term.

The most significant conclusion of the work presented here is that contrary to previous assumptions about the role of fractures in radionuclide retardation, preliminary results from these experiments indicate that fracture flow does not necessarily result in a fast pathway for actinide migration through fractures. As can be seen in the experiments described above, the migration of actinides through fractures could be significantly retarded by sorption onto minerals coating the fractures and by diffusion into the tuff matrix.
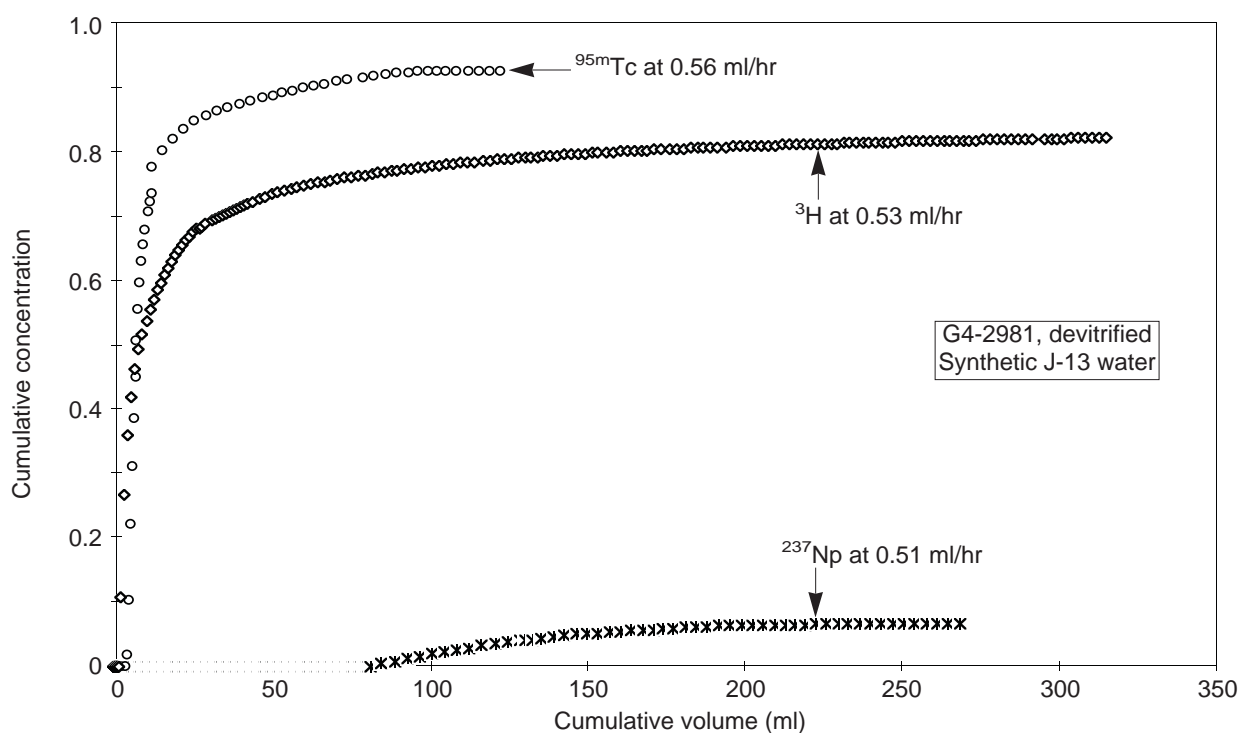
Figure 122. Neptunium and Technetium in Fractured Tuff. The plot shows elution curves for tritium, neptunium-237, and technetium-95m in synthetic J-13 water through a fractured-column of tuff G4-2981.
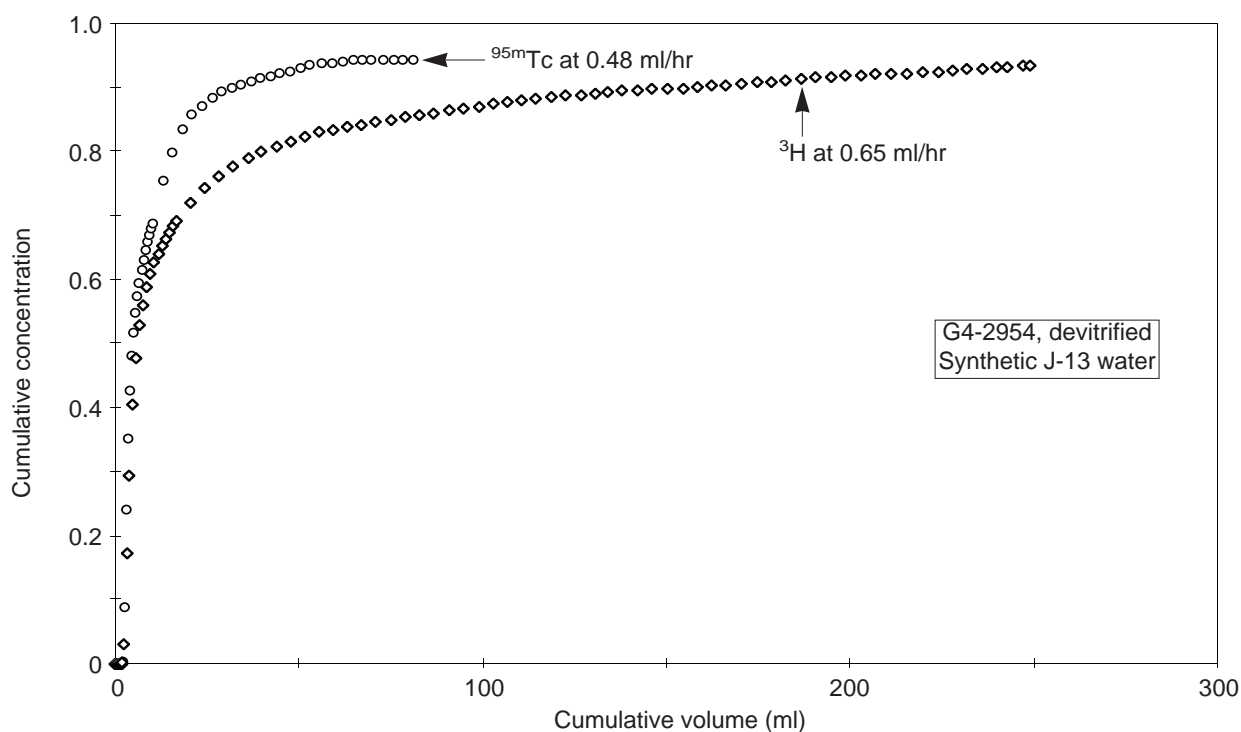
Figure 123. Technetium in Fractured Tuff. The plot shows elution curves for technetium-95m and tritium in synthetic J-13 water through a fractured-column of devitrified tuff G4-2954.

167